Targeted large mass ratio numerical relativity surrogate waveform model for GW190814

Jooheon Yoo[®], ^{1,*} Vijay Varma[®], ^{2,3,1,†} Matthew Giesler[®], ¹ Mark A. Scheel, ⁴ Carl-Johan Haster[®], ^{5,6} Harald P. Pfeiffer, ² Lawrence E. Kidder, ¹ and Michael Boyle¹

¹Cornell Center for Astrophysics and Planetary Science, Cornell University, Ithaca, New York 14853, USA

²Max Planck Institute for Gravitational Physics (Albert Einstein Institute), D-14476 Potsdam, Germany

³Department of Physics, Cornell University, Ithaca, New York 14853, USA

⁴TAPIR 350-17, California Institute of Technology, 1200 East California Boulevard,

Pasadena, California 91125, USA

⁵LIGO Laboratory, Massachusetts Institute of Technology, Cambridge, Massachusetts 02139, USA

⁶Department of Physics and Kavli Institute for Astrophysics and Space Research,

Massachusetts Institute of Technology, 77 Massachusetts Avenue, Cambridge, Massachusetts 02139, USA

(Received 4 April 2022; accepted 29 June 2022; published 1 August 2022)

Gravitational wave observations of large mass ratio compact binary mergers like GW190814 highlight the need for reliable, high-accuracy waveform templates for such systems. We present NRHybsur2dq15, a new surrogate model trained on hybridized numerical relativity (NR) waveforms with mass ratios $q \le 15$ and aligned spins $|\chi_{1z}| \le 0.5$ and $\chi_{2z} = 0$. We target the parameter space of GW190814-like events as large mass ratio NR simulations are very expensive. The model includes the (2, 2), (2, 1), (3, 3), (4, 4), and (5, 5) spin-weighted spherical harmonic modes and spans the entire LIGO-Virgo bandwidth (with $f_{low} = 20$ Hz) for total masses $M \gtrsim 9.5$ M_{\odot} . NRHybsur2dq15 accurately reproduces the hybrid waveforms, with mismatches below $\sim 2 \times 10^{-3}$ for total masses 10 $M_{\odot} \le M \le 300$ M_{\odot} . This is at least an order of magnitude improvement over existing semianalytical models for GW190814-like systems. Finally, we reanalyze GW190814 with the new model and obtain source parameter constraints consistent with previous work.

DOI: 10.1103/PhysRevD.106.044001

I. INTRODUCTION

The LIGO [1] and Virgo [2] detectors have observed a total of 90 gravitational wave (GW) signals to date [3–5], including the landmark observations of the first binary black hole (BH) [6], binary neutron star (NS) [7], and BH-NS binaries [8]. Among these observations, GW190814 [9] is unique due to its uncertain nature: a merger of a \sim 23 M_{\odot} BH and a \sim 2.6 M_{\odot} companion that is either the heaviest NS or the lightest BH ever discovered [9] in a compact binary system. In addition to the intrigue about its astrophysical origin [10–18], this event also poses new challenges for waveform models due to the highly unequal masses of the binary components.

Numerical relativity (NR) is the only available method for solving Einstein's equations near the merger of two compact objects and has played a central role in GW astronomy [19–22]. Unfortunately, NR simulations are prohibitively expensive for direct GW data analysis applications, as each simulation can take up to a few months on a supercomputer. The need for a faster alternative to NR has led to the development of several semianalytical waveform models [23–33] that rely on some physically motivated assumptions for the underlying phenomenology and calibrate the remaining free parameters to NR simulations. As a result, these models are fast enough for GW data analysis, but are typically not as accurate as the NR simulations [34–36].

On the other hand, NR surrogate models [35–38] take a data-driven approach by training the model directly on NR simulations, without the need for added assumptions. These models have been shown to reproduce NR simulations without a significant loss of accuracy while also being fast enough for GW data analysis [35,36]. The main limitation for surrogate models, however, is that their applicability is restricted to the regions where sufficient NR simulations are available. In particular, NR simulations become expensive as one approaches large mass ratios $q = m_1/m_2$ and/or large spin magnitudes $\chi_{1,2}$ [22,39], where m_1 (m_2) represents the mass of the heavier (lighter) BH, so that $q \ge 1$, and $\chi_{1,2}$ represent the corresponding dimensionless spins, with

^{*}iy884@cornell.edu

vijay.varma@aei.mpg.de

 $^{^{1}}$ A similar event, GW200210_092254, a merger of a 24.1 M_{\odot} BH and a 2.81 M_{\odot} compact object was identified in Ref. [5]. However, this event is a marginal GW candidate, with a probability of astrophysical origin $p_{\rm astro} \sim 0.54$ [5]. Therefore, we limit our analysis to GW190814.

magnitudes $\chi_{1,2} \le 1$. Therefore, previous NR surrogate models have only been trained on simulations with $q \le 8$ and $\chi_{1,2} \le 0.8$ [35]. These models are not suitable for highmass ratio systems like GW190814 ($q \sim 8.96^{+0.75}_{-0.62}$ at 90% credibility [9]).

Similarly, the calibration NR data for the semianalytical models [23–26] used in the GW190814 discovery paper [9] are also very sparse at mass ratios $q \gtrsim 8$. Fortunately, most of the events observed by LIGO-Virgo fall at more moderate mass ratios $q \lesssim 5$ [5], with a preference for $q \sim 1$ [40], where current semianalytical models are well calibrated. In contrast, the large mass ratio of GW190814 poses new challenges for waveform modeling, and it is important to understand the impact of modeling error on the source parameter estimation of this event.

For example, at large q, subdominant modes of radiation beyond the quadrupole mode can play an important role. The complex waveform $\hbar = h_+ - ih_\times$ can be decomposed into a sum of spin-weighted spherical harmonic modes $\hbar_{\ell m}$,

$$\mathcal{R}(t, \iota, \varphi_0) = \sum_{l=2}^{\infty} \sum_{m=-\ell}^{\ell} \mathcal{R}_{\ell m}(t)_{-2} Y_{\ell m}(\iota, \varphi_0), \qquad (1)$$

where h_+ (h_\times) represents the plus (cross) GW polarization, $_{-2}Y_{\ell m}$ are the spin = -2-weighted spherical harmonics, and (ι, φ_0) represent the direction to the observer in the source frame. The $\ell=|m|=2$ terms typically dominate the sum in Eq. (1), and are referred to as the quadrupole modes. However, as one approaches large q, the subdominant modes (also referred to as nonquadrupole or higher modes) become increasingly important for estimating the binary source properties [41–45]. Therefore, it is important for waveform models to accurately capture the effect of the subdominant modes on the observed signal. Along with developing a new surrogate model, one of the goals of this work is to assess whether current semianalytical models and, in particular, their subdominant modes are accurate enough for events like GW190814.

A. The NRHybSur2dq15 model

In this work, we build a GW190814-targeted surrogate model that is based on NR simulations with mass ratios up to q=15. Because of the computational cost of NR simulations with large mass ratios and/or spins [22], we restrict the model to spins (anti)aligned along the direction of the orbital angular momentum L, with $\chi_{1z} \in [-0.5, 0.5]$, $\chi_{1x} = \chi_{1y} = 0$, and $\chi_2 = 0$. We ignore the spin of the secondary BH for simplicity, as its effect is expected to be

suppressed for large q systems like GW190814, at least at current signal to noise ratio (SNR). For example, Ref. [9] found that the secondary spin of GW190814 was unconstrained. This assumption may need to be relaxed for louder signals that are expected in the future with detector improvements.

Above, the z direction is taken to be along L, whose direction is constant for aligned-spin systems. In addition to the dominant $[(\ell, m) = (2, 2)]$ mode, the model accurately captures effects of the following subdominant modes: (2,1), (3,3), (4,4), and (5,5). Note that the m < 0 modes carry the same information as m > 0 modes for aligned-spin binaries and do not need to be modeled separately.

To train the model, we perform 20 new NR simulations in the range $8 < q \le 15$, using the spectral Einstein code (SpEC) [22,46] developed by the SXS [47] Collaboration. Because of computational limitations, these simulations only include about 30 orbits before the merger; therefore, they do not cover the full LIGO-Virgo frequency band for stellar mass binaries. More precisely, for total masses $M = m_1 + m_2 \lesssim 70.0 M_{\odot}$, the initial frequency of the (2, 2) mode of these waveforms falls within the LIGO-Virgo band, taken to begin at $f_{low} = 20$ Hz. We extend the validity of the model to lower masses by smoothly transitioning [35] to the effective-one-body (EOB) model SEOBNRv4HM [27] for the early inspiral. These NR-EOB hybrid waveforms are augmented with 31 waveforms in the $q \le 8$ region, generated using the NRHybSur3dq8 [35] surrogate model, which is already hybridized. The new model, NRHybSur2dq15 is trained on these 51 hybrid waveforms, and all modes of this model are valid for the full LIGO-Virgo band (with $f_{low} = 20 \text{ Hz}$) for $M \gtrsim 9.5 M_{\odot}$.

For simplicity, NRHybSur2dq15 ignores two physical features that can be relevant for GW190814: precession and tidal deformability of the secondary object. Precession occurs when the component objects have spins that are tilted with respect to L. In such binaries, the spins interact with L (as well as with each other), causing the orbital plane to precess [48]. The effective precession parameter χ_p [49] for GW190814 was constrained to $\chi_{\rm p} \lesssim 0.07$ at 90% credibility by Ref. [9]. However, including precession in the waveform model was found to improve the component mass constraints [9]. Therefore, while neglecting precession is a reasonable assumption, this can limit the applicability of our results. Precessing NR surrogates can require ≥1000 NR simulations [36,38,50], which is not currently feasible for large mass ratios [22]. Nevertheless, we can still compare the performance of NRHybSur2dq15 against other nonprecessing models.

Next, the tidal deformations of NSs within a compact binary can alter the orbital dynamics, imprinting a signature on the GW signal [51]. Assuming the secondary object of GW190814 is a NS, this effect, parametrized by the effective tidal deformability [51], scales as $\tilde{\Lambda} \propto 1/q^4$

²The source frame is defined as follows: the z axis points along the orbital angular momentum L of the binary, the x axis points along the line of separation from the lighter BH to the heavier BH, and the y axis completes the triad. Therefore, t denotes the inclination angle between L and line of sight to the observer.

[see, e.g., Eq. (1) of Ref. [7]] and can be safely ignored for GW190814 [9]. For large q binaries like GW190814, the NS simply plunges into the BH before tidal deformation or disruption can occur [52]. As a result, GW190814 shows no evidence of measurable tidal effects in the signal and no electromagnetic counterpart to the GWs has been identified [9]. This justifies our choice to ignore the effects of tidal deformation in NRHybSur2dq15.

To summarize, NRHybSur2dq15 is valid for mass ratios $q \le 15$, spins $\chi_{1z} \in [-0.5, 0.5]$ and $\chi_{1x} = \chi_{1y} = \chi_2 = 0$, total masses $M \gtrsim 9.5~M_{\odot}$ (for $f_{\rm low} = 20~{\rm Hz}$), and zero tidal deformability. The name of the model is derived from the fact that it is based on NR hybrid waveforms, spans the two-dimensional parameter space of (q,χ_{1z}) , and extends to q = 15.

The rest of the paper is organized as follows. In Sec. II, we describe the construction of NRHybSur2dq15. In Sec. III, we evaluate the accuracy of the model by computing mismatches against NR-EOB hybrid waveforms. We demonstrate that NRHybSur2dq15 is more accurate than existing semianalytical models by at least an order of magnitude, with mismatches $\lesssim 2 \times 10^{-3}$ throughout its parameter space. In Sec. IV, we reanalyze GW190814 using NRHybSur2dq15 and find that our constraints on the binary properties are consistent with those reported in Ref. [9]. We end with some concluding remarks in Sec. V. Throughout this paper, we denote redshifted detector frame masses as m_1 , m_2 , and $M = m_1 + m_2$. When referring to the source-frame masses, we denote them explicitly as $m_1^{\rm src}$, $m_2^{\rm src}$, and $M^{\rm src}$. These are related by factors of 1 + z, where z is the cosmological redshift; for example, $M = (1 + z)M^{\rm src}$.

II. METHODS

In this section, we describe the steps involved in building the new model NRHybSur2dq15, including the generation of the required NR and hybrid waveforms and the surrogate model construction.

A. Training set generation

In order to build the surrogate model, we need a "training set" of hybrid waveforms and their associated binary parameters. The parameter space of interest for us is the 2D region $q \in [1,15]$ and $\chi_{1z} \in [-0.5,0.5]$, with fixed $\chi_{1x} = \chi_{1y} = 0$, and $\chi_2 = 0$. The total mass scales out for binary BHs and does not need to be modeled separately. The NR simulations necessary for generating hybrid waveforms are expensive, especially as one approaches large q [22]. Therefore, one would ideally like to use the fewest possible hybrid waveforms to build a surrogate model of given a target accuracy. However, we do not know *a priori* how big the training set should be or how these points should be distributed in the parameter space. In order to determine a suitable training set, we first build a surrogate model for post-Newtonian (PN) waveforms.

1. PN surrogate and new NR simulations

We use the GWFrames package [53] to generate PN waveforms. For the orbital phase, we use the TaylorT4 [54] approximant and include nonspinning terms up to 4 PN order [55–58] and spin terms up to 2.5 PN order [59–61]. For the amplitudes, we include terms up to 3.5 PN order [62–64]. For the PN surrogate, we restrict the length of the waveforms to be 5000 M, terminating at the orbital frequency of the Schwarzschild innermost-stable circular orbit (ISCO): $\omega_{\rm orb} = 6^{-3/2} \, {\rm rad}/M$. In addition, we only use the (2, 2) mode for simplicity. Despite the restrictions in length, mode content, and the missing merger-ringdown section in the PN waveforms, we find that this approach provides a good initial training set for constructing hybrid NR-EOB surrogates [35]. Above, the orbital frequency is defined as

$$\omega_{\rm orb} = \frac{d\phi_{\rm orb}}{dt},\tag{2}$$

where ϕ_{orb} is the orbital phase obtained from the (2, 2) mode [see Eq. (8)].

We initialize the training set for the PN surrogate with just the corner cases of the parameter space. For our 2D model, these consist of the four points: $(q, \chi_{1z}) = (1, \pm 0.5)$ and $(15, \pm 0.5)$. We augment the training set in an iterative *greedy* manner: At each iteration, we build a PN surrogate with the current training set, following the same methods as we use for the hybrid surrogate (see Sec. II D). Then, we test this surrogate against a larger (~ 10 times) "validation set," generated by randomly sampling the parameter space at each iteration. We select the parameter in the validation set that has the largest error [computed using Eq. (4)] and add it to the training set for the next iteration. We repeat this procedure until the largest validation error falls below a certain threshold.

In order to estimate the error between two complex waveforms \mathcal{R}_1 and \mathcal{R}_2 , we use the time-domain inner product,

$$\langle \mathcal{R}_1, \mathcal{R}_2 \rangle = \left| \int_t^{t_{\text{max}}} \mathcal{R}_1(t) \mathcal{R}_2^*(t) dt \right|,$$
 (3)

to compute the mismatch

$$\mathcal{M}\mathcal{M} = 1 - \frac{\langle \hat{n}_1, \hat{n}_2 \rangle}{\sqrt{\langle \hat{n}_1, \hat{n}_1 \rangle \langle \hat{n}_2, \hat{n}_2 \rangle}}.$$
 (4)

When computing mismatches for the PN surrogate, we assume a flat noise curve and do not optimize over time and phase shifts.

³The boundary parameters are expected to be more important than those in the bulk; therefore, for 30% of the points in the validation set, we sample only from the boundary, which corresponds to the edges of a square in the 2D case.

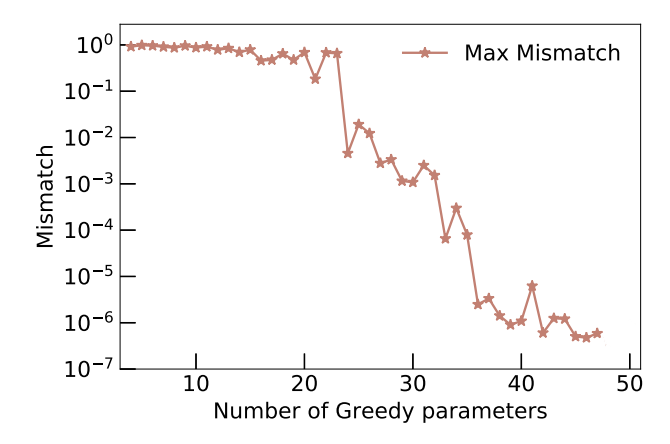


FIG. 1. Largest mismatch of the PN surrogate (over the entire validation set) as a function of number of greedy parameters used for training. The PN surrogate is seen to converge to the validation waveforms as the size of the training set increases.

Figure 1 shows the maximum validation error at each iteration against the size of the training set. We stop this procedure when the training set size reaches 47, as the mismatch settles below 10^{-6} at this point. Among these, 31 cases lie in the region $q \le 8$, while 16 lie in the region $8 < q \le 15$. Rather than perform new NR simulations for the $q \le 8$ cases, we generate waveforms using the existing NRHybSur3dq8 model [35]. This model was trained on NR-EOB/PN hybrid waveforms with mass ratios $q \le 8$ and spins $\chi_{1z,2z} \in [-0.8,0.8]$ and was shown to reproduce the hybrid waveforms without a significant loss of accuracy [35].

For the cases with q > 8, we perform new NR simulations using SpEC [22,46]. These NR waveforms include $\sim 5000M$ of evolution before the merger and are hybridized using SEOBNRv4HM [27] waveforms to include the early inspiral (see Sec. II A 2). However, of the 16 cases with q > 8, only 15 simulations were successfully completed. This leaves us with a total of 46 training waveforms (15 NR-EOB hybrid waveforms and 31 NRHybSur3dq8 waveforms).

From an initial attempt to build a hybrid surrogate with these 46 waveforms, we found that the model performs poorly for low masses $\lesssim 50~M_{\odot}$, with mismatches reaching $\sim 10^{-2}$, but performs very well for higher masses, with mismatches $\sim 10^{-3}$. In other words, the late inspiral and merger-ringdown stages were accurately captured, but the early inspiral was not. This suggested that more hybrid waveforms were required. To estimate where in parameter space to place new hybrid waveforms, we first constructed a trial NR-only surrogate using the above training set of 46 waveforms, but restricted to the last 5000 M before merger;

we will refer to this model as NRSur2dq15. Next, we hybridized waveforms (see Sec. II A 2) obtained from NRSur2dq15 to generate new training points in the q > 8 region. This bootstrap method allowed us to create as many hybrid waveforms as necessary in the q > 8 region without performing new NR simulations. After some trial and error, we found that placing five new hybrid waveforms at q = 14 (uniformly distributed in $\chi_{1z} \in [-0.5, 0.5]$) resolved the problem at low masses.

With this insight, we finally performed five new SpEC NR simulations at these points and added the hybrid waveforms based on these to our training set for the final model, which now includes 20 NR-EOB hybrid waveforms and 31 NRHybSur3dq8 waveforms, for a total of 51 waveforms. Figure 2 shows the distribution of these parameters, including the failed simulation and the new q=14 simulations.

The new NR simulations are performed using SpEC [22,46]; they have been assigned identifiers SXS:BBH: 2463-SXS:BBH:2482 and made publicly available through the SXS catalog [65]. The constraint equations are solved employing the extended conformal thin sandwich formalism [66,67] with superposed harmonic Kerr free data [68]. The evolution equations are solved employing the generalized harmonic formulation [69,70]. The start time of these simulations is approximately 5000 M before the peak of the waveform amplitude [defined in Eq. (5)], where $M = m_1 + m_2$ is the total Christodoulou mass measured after the initial burst of junk radiation [22]. The initial orbital parameters are chosen through an iterative procedure [71] such that the orbits are quasicircular; the largest eccentricity for these simulations is 6.4×10^{-4} , while the

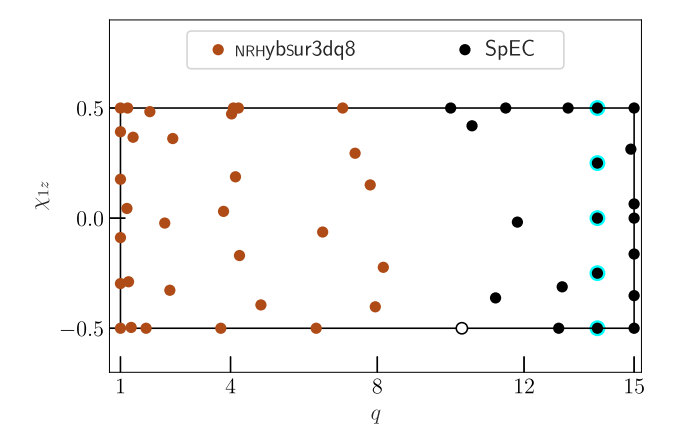


FIG. 2. Training set parameters used in building the surrogate model NRHybSur2dq15. The red markers correspond to cases with $q \le 8$, for which NRHybSur3dq8 is used to generate training waveforms. The black markers represent the new NR waveforms performed for this work, while the empty marker shows the failed NR simulation. The distribution of the 47 parameters from Fig. 1 can be seen by ignoring the black markers highlighted in cyan; these represent the five additional NR simulations that were necessary to improve the model.

⁴The reason for failure is large constraint violation as the binary approaches merger. We believe a better domain decomposition may be needed for this simulation, which we plan to explore in the future.

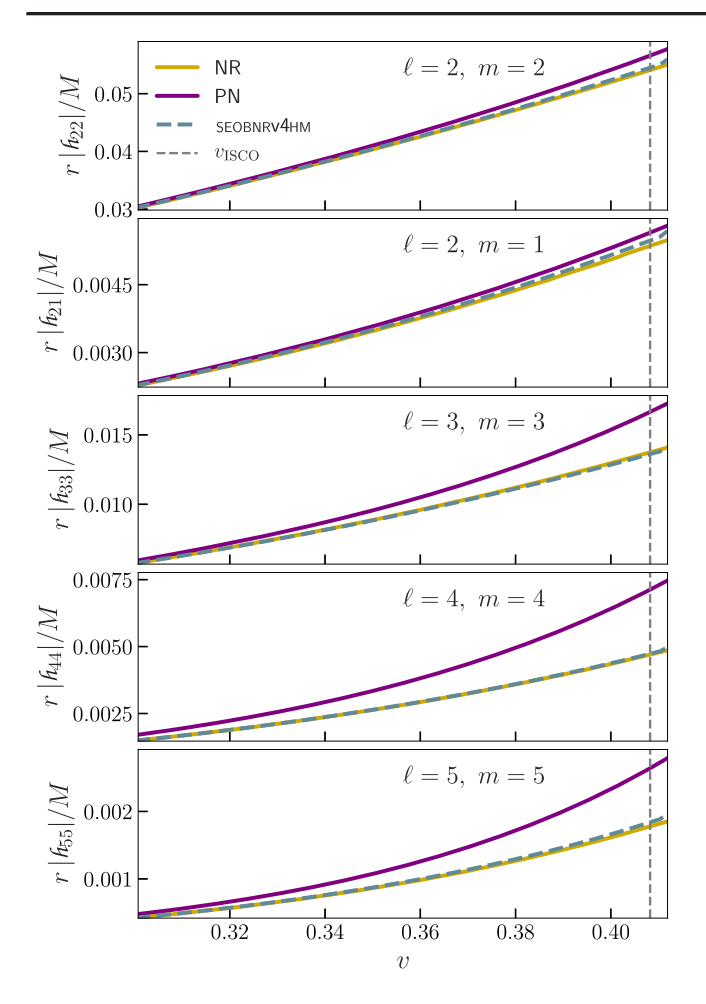


FIG. 3. Mode amplitudes for NR, PN, and SEOBNRv4HM as a function of the characteristic speed $v=\omega_{\rm orb}^{1/3}$ for binary parameters $(q,\chi_{1z},\chi_{2z})=(15,0.5,0.0)$. The vertical dashed lines represent the Schwarzschild ISCO point $v=1/\sqrt{6}$. While PN deviates significantly from NR, SEOBNRv4HM shows excellent agreement. We show all available modes of SEOBNRv4HM.

median value is 2.9×10^{-4} . The waveforms are extracted at several extraction surfaces at varying finite radii form the origin and then extrapolated to future null infinity [72]. Finally, the extrapolated waveforms are corrected to account for the initial drift of the center of mass [73].

2. Hybridization

Given the new NR waveforms, we now hybridize them by smoothly attaching an EOB waveform for the early inspiral. For the previous NR hybrid surrogate model NRHybSur3dq8 [35], a combination of PN and EOB was used for the early inspiral: the amplitudes for all modes were obtained from PN, while the phase evolution for all modes was derived from the (2, 2) mode of the SEOBNRv4 EOB model [74] (see Sec. IV B of Ref. [35]). This was motivated by the fact that the PN mode amplitudes were found to be accurate enough for hybridizing $q \le 8$ NR

simulations, while the PN mode phases were not (see Fig. 3 of Ref. [35]).

We find that the same strategy does not work for the large q cases considered in this work. Figure 3 shows a comparison between the mode amplitudes of NR, PN, and the SEOBNRv4HM EOB model [27], for a q = 15 system. We show all modes [(2, 2), (2, 1), (3, 3), (4, 4), and (5, 5)]included by SEOBNRv4HM, which is an extension of the SEOBNRv4 model. The PN waveforms are described in Sec. II A 1; we include amplitude terms up to 3.5 PN order [62-64]. In Fig. 3, the PN amplitudes (especially for the subdominant modes) deviate significantly from NR, while SEOBNRv4HM shows excellent agreement. This is not surprising, as SEOBNRv4HM is calibrated to NR waveforms, as well as some BH perturbation theory waveforms at extreme mass ratios [27]. We conclude that current PN waveforms are not suitable for hybridizing NR waveforms at large mass ratios like $q \sim 15$. Therefore, in this work, we only use SEOBNRv4HM for hybridizing NR waveforms. Unfortunately, this means that our new model NRHybSur2dq15 is restricted to the same set of modes as SEOBNRv4HM.

We follow the same hybridization procedure as Sec. V of Ref. [35] to smoothly attach SEOBNRv4HM inspirals to the 20 new q>8 NR simulations obtained in Sec. II A 1. For the remaining 31 training cases with $q\leq 8$, we generate waveforms using the NRHybSur3dq8 model, as it is already hybridized. This completes the construction of our training set of waveforms.

B. Frame alignment

We follow Ref. [35] and apply the following postprocessing to the training set waveforms. This ensures that all waveforms are in the same frame, and therefore that the data used in the surrogate fits (see Sec. II D) vary smoothly across parameter space.

1. Time alignment

We apply a time shift to each training waveform such that the peak of the total amplitude

$$A_{\text{tot}} = \sqrt{\sum_{l,m} |\mathcal{R}_{\ell m}|^2} \tag{5}$$

occurs at t = 0. The original peak time is determined by a quadratic fit using five time samples adjacent to the discrete maximum of A_{tot} [38].

2. Downsampling and common time array

The length of each hybrid waveform is set by choosing a starting orbital frequency $\omega_{\rm orb}$ for the SEOBNRv4HM inspiral; we use $\omega_{\rm orb} = 1 \times 10^{-3} \ {\rm rad}/M$ for all waveforms. However, for the same starting frequency, the waveform length in time is different for different mass ratios and

spins. On the other hand, the surrogate modeling procedure requires that all training waveforms have a common time array [37]. Therefore, we truncate all waveforms such that they start at the same initial time ($\sim 2.4 \times 10^7 M$ before the peak), which is determined by the shortest hybrid waveform in the training set. Post truncation, the largest starting orbital frequency is $\omega_{\rm orb} = 1.1 \times 10^{-3} \, {\rm rad}/M$, which sets the low-frequency limit of validity of the surrogate. For LIGO and Virgo, assuming a starting GW frequency of 20 Hz, the (2, 2) mode of the surrogate model is valid for total masses $M \ge 3.7 \, M_{\odot}$. The highest spin-weighted spherical harmonic mode included in the model is (5, 5), for which the corresponding frequency is 5/2 times that of the (2, 2) mode. Therefore, all modes of the surrogate are valid for $M \gtrsim 9.5 \, M_{\odot}$.

Because the hybrid waveforms are very long, it is not practical to sample the entire waveform with a small uniform time step like 0.1 M, as is typically done for NR-only surrogates [36]. Fortunately, the early lowfrequency portion of the waveform does not require as dense a time sampling as the later high-frequency portion. We therefore downsample the time arrays of the truncated hybrid waveforms to a common set of time samples. We choose the time samples such that there are five points per orbit for the above-mentioned shortest hybrid waveform in the training set. However, for $t \ge -1000 M_{\odot}$, we switch to uniformly spaced time samples with a time step of 0.1 M. This ensures that we have a sufficiently dense sampling rate for the late inspiral and the merger ringdown where the frequency reaches its peak. We retain times up to 120M after the peak, which is sufficient to capture the entire ringdown.

Given the common downsampled time array, we use cubic splines to interpolate all waveforms in the training set to these times. However, we first transform the waveforms into the co-orbital frame, defined as

$$\hbar_{\ell m}^{C} = \hbar_{\ell m} e^{im\phi_{\text{orb}}},$$
(6)

$$\mathcal{R}_{22} = A_{22} e^{-i\phi_{22}},\tag{7}$$

$$\phi_{\rm orb} = \frac{\phi_{22}}{2},\tag{8}$$

where $\mathcal{R}_{\ell m}$ is the inertial frame waveform, $\phi_{\rm orb}$ is the orbital phase, and A_{22} and ϕ_{22} are the amplitude and phase of the (2, 2) mode. The co-orbital frame can be seen as roughly corotating with the binary, obtained by applying a time-dependent rotation about the z axis, by an amount given by the instantaneous orbital phase. Therefore, the waveform is a slowly varying function of time in this frame, which increases the interpolation accuracy. For the (2, 2) mode we save the downsampled amplitude A_{22} and phase ϕ_{22} , while for all other modes we save the real and imaginary parts of $\mathcal{R}_{\ell m}{}^{C}$.

3. Phase alignment

Finally, we rotate the waveforms about the z axis such that the orbital phase $\phi_{\rm orb}$ is zero at t=-1000~M. Note that this by itself would fix the physical rotation up to a shift of π . When generating the EOB inspiral waveform for hybridization, the frame is aligned such that heavier BH is on the positive x axis at the initial time, which fixes the π ambiguity [35]. After the phase alignment, the heavier BH is on the positive x axis at t=-1000~M for all waveforms. However, keep in mind that this frame is defined using the waveform at future null infinity, and these BH positions do not necessarily correspond to the (gauge-dependent) coordinate BH positions in the NR simulations.

C. Data decomposition

It is much easier to build a model for slowly varying functions of time. Therefore, we decompose the inertial frame strain $\mathcal{R}_{\ell m}$, which is oscillatory, into simpler "waveform data pieces" and build a separate surrogate for each data piece. When evaluating the full surrogate model, we first evaluate the surrogate for each data piece and then combine the data pieces to get the inertial frame strain. The (2, 2) mode is decomposed into its amplitude A_{22} and phase ϕ_{22} (which is further decomposed below). For the other modes, we model the real and imaginary parts of the co-orbital frame strain $\mathcal{R}_{\ell m}{}^{\mathcal{C}}$ [see Eq. (6)].

Following Ref. [36], we further decompose ϕ_{22} by subtracting the leading-order prediction from the TaylorT3 PN approximant [75], given by

$$\phi_{22}^{\text{T3}} = \phi_{\text{ref}}^{\text{T3}} - \frac{2}{n\theta^5},$$
 (9)

where $\phi_{\rm ref}^{\rm T3}$ is an arbitrary integration constant, $\theta = [\eta(t_{\rm ref}-t)/(5M)]^{-1/8}$, $t_{\rm ref}$ is an arbitrary time offset, and $\eta = q/(1+q)^2$ is the symmetric mass ratio. Because $\phi_{\rm ref}^{\rm T3}$ diverges at $t_{\rm ref}$, we choose $t_{\rm ref} = 1000M$, long after the peak (t=0) of the waveform, ensuring that we are always far away from this divergence. We choose $\phi_{\rm ref}^{\rm T3}$ such that $\phi_{22}^{\rm T3} = 0$ at t = -1000~M, which is the same time at which we align the hybrid phase in Sec. II B 3.

By modeling the difference $\phi_{22}^{\rm res} = \phi_{22} - \phi_{22}^{\rm T3}$ instead of ϕ_{22} , we automatically capture almost all of the phase evolution in the early inspiral of the long hybrid waveforms. Therefore, we simplify the problem of modeling the phase to the same as modeling the phase of NR-only waveforms. This improves the overall accuracy of the surrogate model for low masses, for which the inspiral dominates. We stress that the exact form of $\phi_{22}^{\rm T3}$ (or its physical meaning) is not important because we add the exact same $\phi_{22}^{\rm T3}$ to our model of $\phi_{22}^{\rm res}$ when evaluating the surrogate. In fact, even though TaylorT3 is known to be less accurate than other approximants [76,77], its speed (being a

simple, analytic, closed-form, function of time) makes it ideal for our purpose.

To summarize, we decompose the hybrid waveforms into the following waveform data pieces, each of which is a smooth, slowly varying function of time: $(A_{22}, \phi_{22}^{\text{res}})$ for the (2, 2) mode and the real and imaginary parts of $\mathcal{M}_{\ell m}^{C}$ for the (2, 1), (3, 3), (4, 4), and (5, 5) modes.

D. Surrogate construction and evaluation

Given the waveform data pieces, we build a surrogate model for each data piece using the same procedure as Sec. V C of Ref. [35], which we summarize below.

For each waveform data piece, we first construct a linear basis using the greedy basis method [78], with tolerances of 10^{-2} rad for the $\phi_{22}^{\rm res}$ data piece and 5×10^{-5} for all other data pieces. Next, we construct an empirical time interpolant [79–81] with the same number of empirical time nodes as basis functions for that data piece. Finally, for each empirical time node, we construct a parametric fit for the waveform data piece, following the Gaussian process regression fitting method, as described in Refs. [82,83]. The fits are parametrized by $(\log(q), \hat{\chi})$, where

$$\hat{\chi} = \frac{\chi_{\text{eff}} - 38\eta(\chi_{1z} + \chi_{2z})/113}{1 - 76\eta/113} \tag{10}$$

is the spin parameter entering the GW phase at leading order [84], and $\chi_{\rm eff} = \frac{q\chi_{1z} + \chi_{2z}}{1+q}$ is the effective spin. Note that in the above expressions $\chi_{2z} = 0$ for the current surrogate, but we adopt this parametrization to be consistent with Ref. [35]. In practice, parametrizing the fits by $(\log(q), \chi_{1z})$ also leads to a surrogate of similar accuracy. On the other hand, the $\log(q)$ parametrization leads to a significant improvement in model accuracy, in agreement with Refs. [35,85].

When evaluating the surrogate waveform, we first evaluate each surrogate waveform data piece. Next, we compute the (2, 2) mode phase,

$$\phi_{22}^{S} \equiv \phi_{22}^{\text{res,S}} + \phi_{22}^{\text{T3}}, \tag{11}$$

where $\phi_{22}^{\rm res,S} \approx \phi_{22}^{\rm res}$ is the surrogate model for $\phi_{22}^{\rm res}$, and $\phi_{22}^{\rm T3}$ is given by Eq. (9). If the waveform is required at a uniform sampling rate, we interpolate each waveform data piece from the sparse time samples to the required time samples using a cubic-spline interpolation scheme. Finally, we use Eqs. (6)–(8) to reconstruct the inertial frame strain.

III. SURROGATE ERRORS

In this section, we evaluate the accuracy of NRHybSur2dq15 by comparing against NR-EOB hybrid waveforms. Similarly, we compute errors for two semianalytic waveform models, the phenomenological model IMRPhenomTHM

[29] and the EOB model SEOBNRv4HM [27]. Both of these models are calibrated against nonprecessing NR simulations and include the same set of modes as NRHybSur2dq15 and the hybrid waveforms: (2, 2), (2, 1), (3, 3), (4, 4), and (5, 5). Other semianalytic nonprecessing models that include subdominant modes exist in literature, including Refs. [31,33], but we do not consider these models for simplicity (as they have accuracies comparable [31,33,86] to IMRPhenomTHM and SEOBNRv4HM).

In order to estimate the difference between two waveforms \mathcal{R}_1 and \mathcal{R}_2 , we compute the mismatch [Eq. (4)] using the noise-weighted inner product in frequency domain, defined as

$$\langle \mathcal{R}_1, \mathcal{R}_2 \rangle = 4\Re \left[\int_{f_{\min}}^{f_{\max}} \frac{\tilde{\mathcal{R}}_1(f)\tilde{\mathcal{R}}_2^*(f)}{S_n(f)} df \right], \qquad (12)$$

where $\tilde{R}(f)$ indicates the Fourier transform of the complex strain R(t), * indicates a complex conjugation, R(t) is the one-sided power spectral density of a GW detector. We use the advanced-LIGO design sensitivity zero-detuned, high-power noise curve [87], with $f_{\text{min}} = 20$ and $f_{\text{max}} = 2000$ Hz. We compute the mismatches following the procedure described in Sec. VII of Ref. [35]: the mismatches are optimized over shifts in time, polarization angle, and initial orbital phase. Both plus and cross polarizations are treated on an equal footing by using a two-detector setup, where one detector sees only the plus and the other only the cross polarization. We use all the available modes of a given waveform model and compute the mismatches at 37 points uniformly distributed on the sky in the source frame.

Figure 4 shows mismatches computed using the advanced-LIGO noise curve for NRHybSur2dq15, SEOBNRv4HM, and IMRPhenomTHM against hybrid waveforms. As these depend on the total mass, we show mismatches for various masses, starting near the lower limit of the range of validity of the surrogate $M \gtrsim 9.5~M_{\odot}$. At each mass, we show the median and 95th percentile mismatches, over many hybrid waveforms and points in the source-frame sky.

The left panel of Fig. 4 shows mismatches against the 20 q > 8 NR-EOB hybrid waveforms in Fig. 2. As these hybrid waveforms were also used in the training of NRHybSur2dq15, we conduct a "leave-one-out" analysis: we generate 20 trial surrogates, leaving out one of the q > 8 hybrid waveforms from the training set in each trial, but including the rest of the training cases (both q > 8 and $q \le 8$) in Fig. 2. For each trial surrogate, we compute errors against the q > 8 hybrid waveform that was left out. In this manner, we only compare NRHybSur2dq15 against waveforms not used in the model training. Therefore, these errors are indicative of the true modeling error.

For the q > 8 region, 95th percentile mismatches for NRHybSur2dq15 fall below $\sim 2 \times 10^{-3}$ over the entire mass

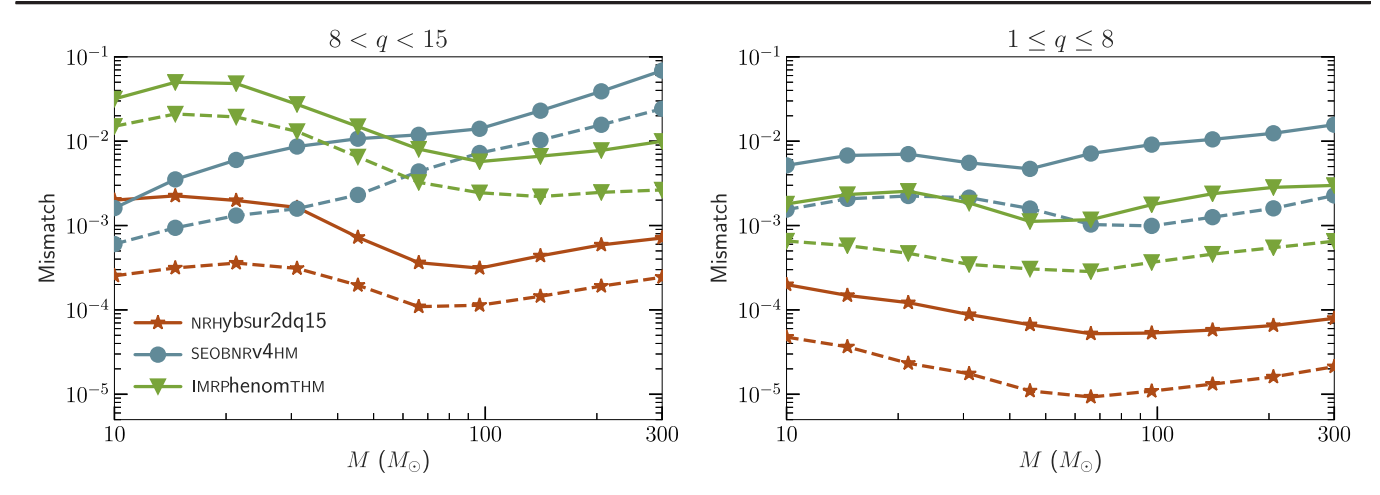


FIG. 4. Left: mismatches as a function of the total mass M for NRHybsur2dq15, SEOBNRv4HM, and IMRPhenomTHM against NR-EOB hybrid waveforms with q > 8. For NRHybsur2dq15, we show leave-one-out errors. Mismatches are computed using the advanced-LIGO noise curve, at several points in the sky of the source frame using all available modes: (2, 2), (2, 1), (3, 3), (4, 4), and (5, 5). The solid (dashed) lines show the 95th percentile (median) mismatch values over points on the sky, as well as different hybrid waveforms. Right: same, but now the mismatches are computed against the NRHybsur3dq8 model in the $q \le 8$ region.

range in Fig. 4. The errors for IMRPhenomTHM and SEOBNRv4HM are generally larger by at least an order of magnitude. However, for SEOBNRv4HM, the errors at low masses overlap with the surrogate errors. This is most likely because SEOBNRv4HM was used to generate the early inspiral waveform for the NR-EOB hybrid waveforms. At low masses, where the early inspiral dominates the overall error budget, these errors are therefore not representative of the true error in SEOBNRv4HM.

The right panel of Fig. 4 shows mismatches in the q < 8 region. In this region, rather than conduct leave-one-out tests, we simply generate 100 new hybrid waveforms using the NRHybSur3dq8 model for testing. These test cases are uniformly distributed in the region $q \in [1,8]$ and $\chi_{1z} \in [-0.5,0.5]$, with $\chi_{2z} = 0$. Once again NRHybSur2dq15 has mismatches that are at least an order of magnitude smaller than that of SEOBNRv4HM and IMRPhenomTHM. In this case, SEOBNRv4HM errors are broadly uniform across all masses. This is most likely explained by the fact that the early inspiral of NRHybSur3dq8 was based on PN as well as EOB waveforms; more precisely, PN was directly used to generate the mode amplitudes, while the (2, 2) mode of SEOBNRv4HM (the SEOBNRv4 [74] model) was used to correct the PN mode phases.

While Fig. 4 shows model errors when including all available modes, it can be useful to also understand the errors in the individual modes. We quantify this using the normalized L_2 norm between two waveforms \hbar and \hbar' ,

$$\mathcal{E}(\hbar, \hbar') = \frac{1}{2} \frac{\sum_{l,m} \int_{t_1}^{t_2} |\mathcal{R}_{\ell m}(t) - \mathcal{R}'_{\ell m}(t)|^2 dt}{\sum_{l,m} \int_{t_1}^{t_2} |\mathcal{R}_{\ell m}(t)|^2 dt}.$$
 (13)

This error measure was introduced in Ref. [50] and is related to weighted average of the mismatch over the sky in the source frame. When computing \mathcal{E} , we only consider the late inspiral and merger-ringdown region by choosing $t_1 =$ -4500 M and $t_2 = 115 M$. As the NR waveforms used in generating the hybrid waveforms had typical start times $\sim -5000 M$ (see Sec. II A), this ensures that \mathcal{E} is independent of which model was used in the hybridization procedure. Furthermore, rather than optimizing over time or phase shifts, we simply align the frames of the two waveforms such that the peak amplitude [Eq. (5)] occurs at t = 0, and the orbital phase [Eq. (8)] is zero at t = -4500M. This makes \mathcal{E} much cheaper to evaluate than the mismatches in Eq. (12). In addition to computing normalized errors using all available modes, we also consider single-mode errors by restricting the sums in Eq. (13) to individual modes.

Figure 5 shows normalized errors for NRHybSur2dq15, SEOBNRv4HM, and IMRPhenomTHM against hybrid waveforms. The left panel of Fig. 5 follows the left panel of Fig. 4 and shows errors for the three waveform models (using a leave-one-out analysis for NRHybSur2dq15) against the 20 q > 8 NR-EOB hybrid waveforms. The right panel of Fig. 5 follows the right panel of Fig. 4 and shows errors against the same 100 uniformly distributed NRHybSur3dq8 waveforms in the region $q \in [1,8]$ and $\chi_{1z} \in [-0.5,0.5]$, with $\chi_{2z} = 0$. For both q > 8 and $q \le 8$, we once again find that NRHybSur2dq15 is more accurate than the other models by at least an order of magnitude, both for the full waveform and for the individual modes.

Considering the individual mode errors in Fig. 5, we note that the fractional errors in the nonquadrupole modes

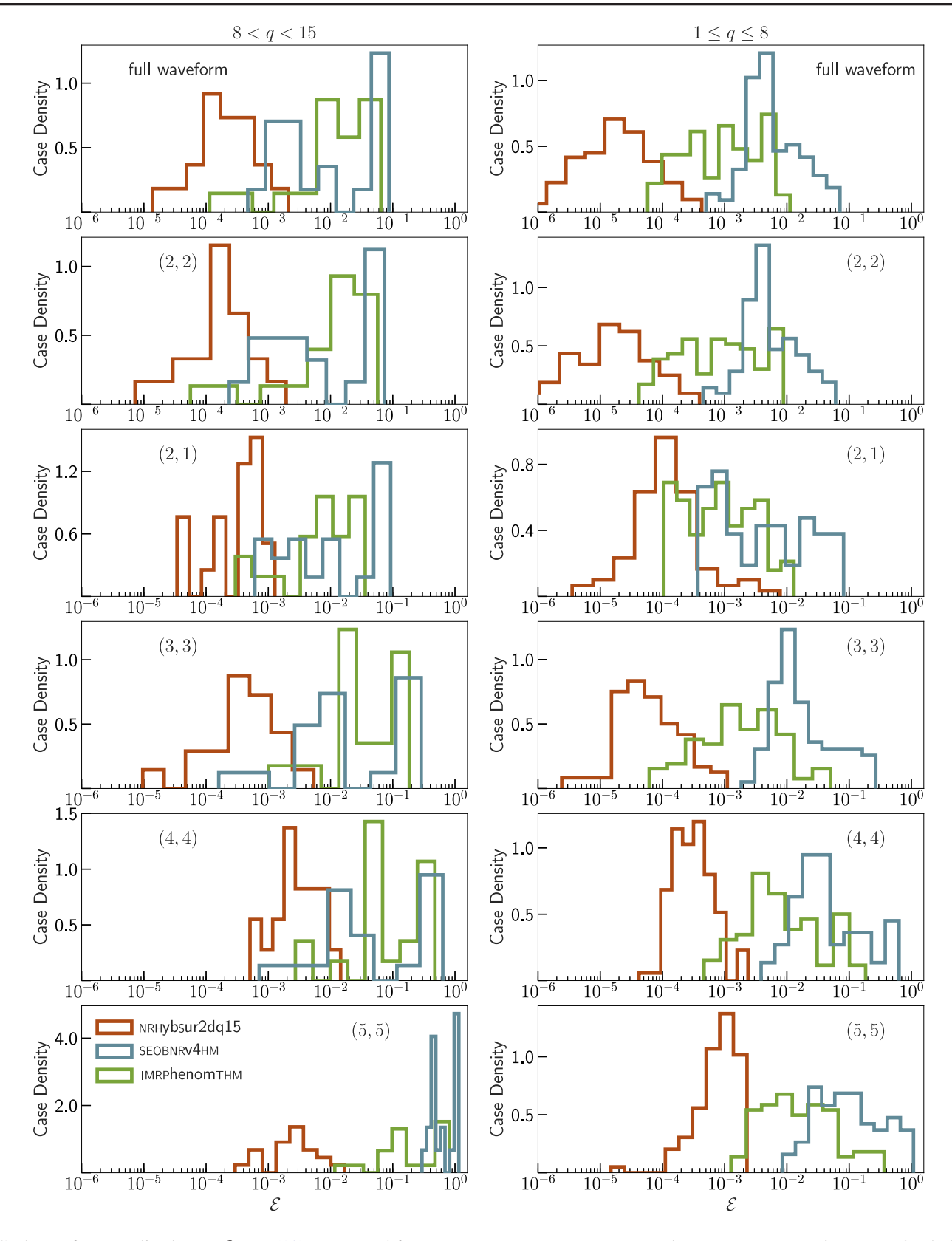


FIG. 5. Left: normalized error \mathcal{E} [Eq. (13)] computed for NRHybsur2dq15, SEOBNRv4HM, and IMRPhenomTHM against NR-EOB hybrid waveforms with q > 8, but restricting the start time of the waveforms to -4500M before the peak amplitude. In the first row, \mathcal{E} is computed using all available modes, and in the subsequent rows, single-mode errors are computed by restricting Eq. (13) to individual modes. Right: same, but now the error is computed against the NRHybsur3dq8 model in the $q \le 8$ region.

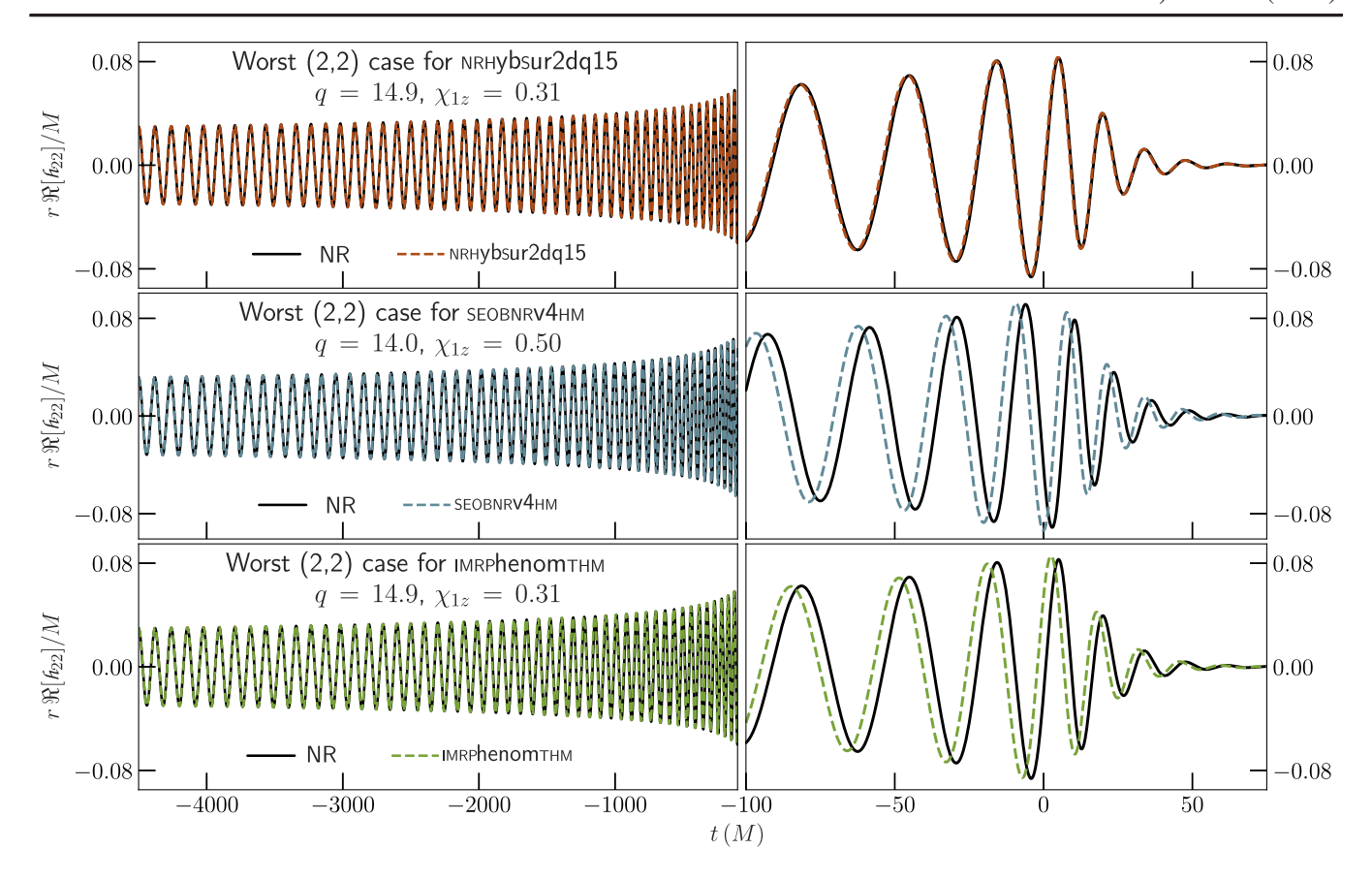


FIG. 6. The (2, 2) modes of the three waveform models compared against NR, for the cases that lead to the largest (2, 2) mode error in the left panel of Fig. 5. The top (middle) [bottom] figure shows the case for which NRHybSur2dq15 (SEOBNRv4HM) [IMRPhenomTHM] has the largest (2, 2) mode error.

of SEOBNRv4HM and IMRPhenomTHM reach large values. In particular, the errors in the (5, 5) mode for SEOBNRv4HM for q>8 can reach values $\mathcal{E}\sim 1$. While the nonquadrupole modes are still subdominant for $q\gtrsim 10$ binaries like GW190814 (which is why the full waveform errors do not reach such large values in Fig. 5), it may be important for models like IMRPhenomTHM and SEOBNRv4HM to improve accuracy in these modes for future observations. Finally, to illustrate the (in)accuracy of the individual modes, Figs. 6–8 show the cases leading to the largest individual mode errors in the left panel of Fig. 5.

A. Extrapolating outside the training region

The errors computed so far were restricted to the training region of NRHybSur2dq15: $q \le 15$, $\chi_{1z} \in [-0.5, 0.5]$, and $\chi_{2z} = 0$. It is possible to extrapolate the model to larger q and $|\chi_{1z}|$, but it is difficult to assess the model accuracy in this region due to a lack of NR simulations. Instead, through a visual inspection of the evaluated waveforms, we find that extrapolating beyond q = 20 or $|\chi_{1z}| = 0.7$ leads to unphysical "glitches" in the time series for the mode amplitudes and the derivatives of the mode phases. Therefore, while we allow the model to be evaluated in the

region $q \le 20$, $\chi_{1z} \in [-0.7, 0.7]$, and $\chi_{2z} = 0$, we advise caution when extrapolating the model.

IV. REANALYZING GW190814

NRHybSur2dq15 is targeted towards GW events like GW190814 [9], with mass ratios $q \gtrsim 9$. As NRHybSur2dq15 is more accurate than alternative models in this region, we now reanalyze GW190814 with NRHybSur2dq15. In addition, we consider two phenomenological models, IMRPhenomTHM [29] and IMRPhenomTPHM [28]. Both of these models include the effects of subdominant modes, but only IMRPhenomTPHM includes precession effects. Precession effects are included in IMRPhenomTPHM by "twisting" the frame of the nonprecessing model IMRPhenomTHM to mimic orbital precession [28]. The GW190814 discovery paper [9] instead considered the SEOBNRv4PHM [23] and IMRPhenomPv3PHM [24] binary BH models, both of which include the effects of subdominant modes and precession (through a similar twisting procedure). For simplicity, we do not consider these models here, but we have verified that our results with IMRPhenomTPHM are consistent with Ref. [9]. Reference [9] also considered models [25,26] with tidal effects, but found no measurable tidal signatures; therefore, we only show results for binary BH models.

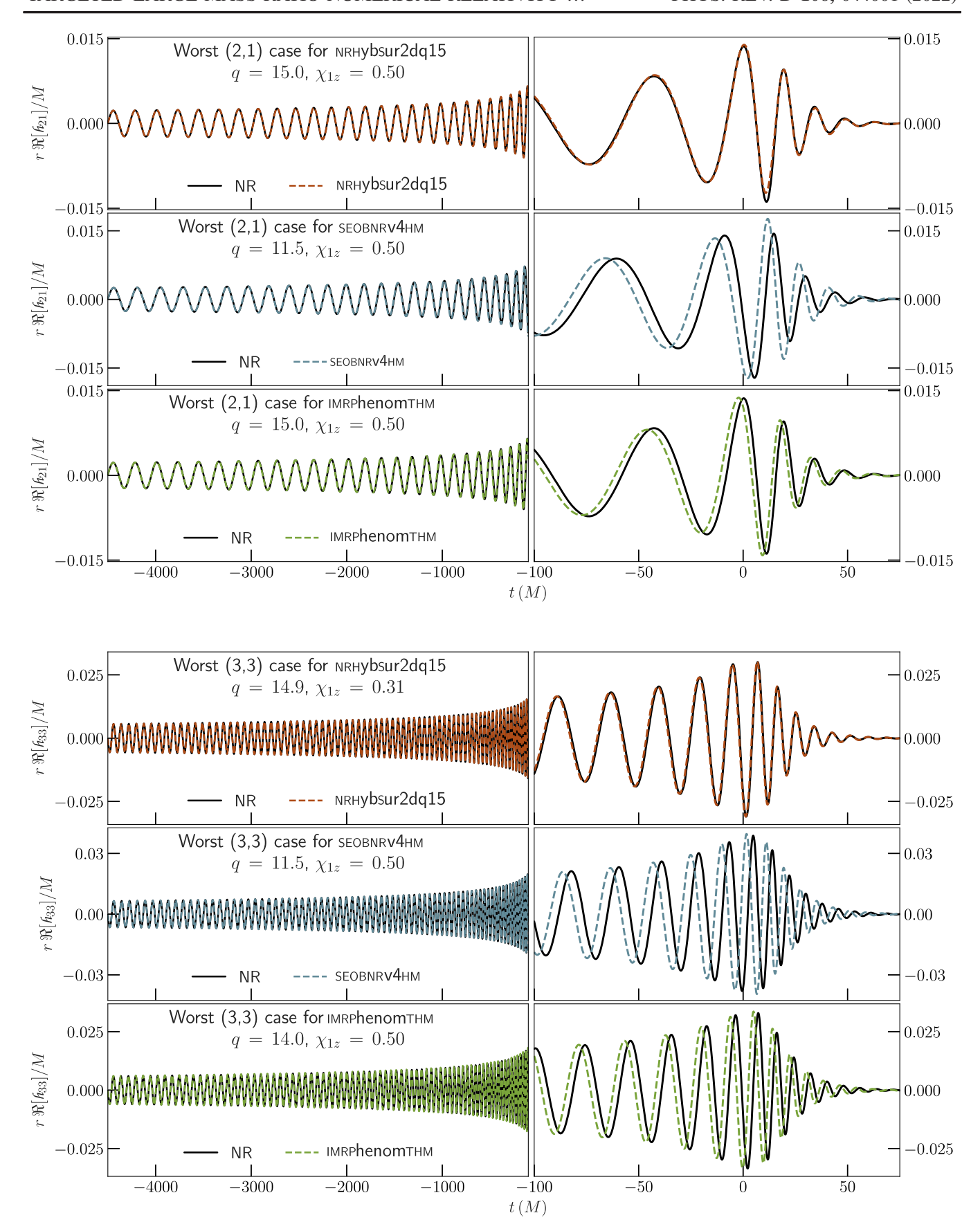


FIG. 7. Same as Fig. 6, but now showing the worst cases for the (2, 1) (top) and (3, 3) (bottom) modes.

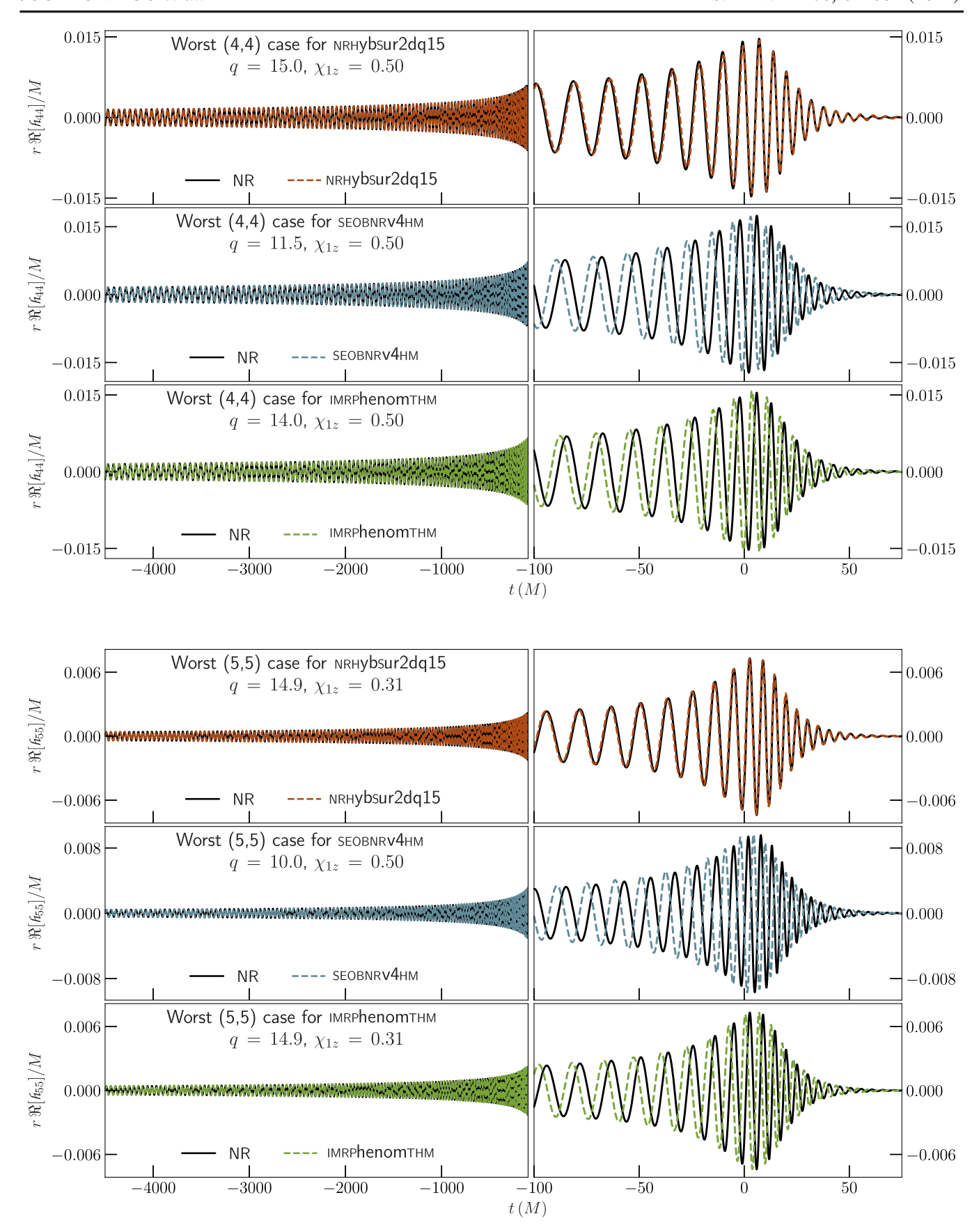


FIG. 8. Same as Fig. 6, but now showing the worst cases for the (4, 4) (top) and (5, 5) (bottom) modes.

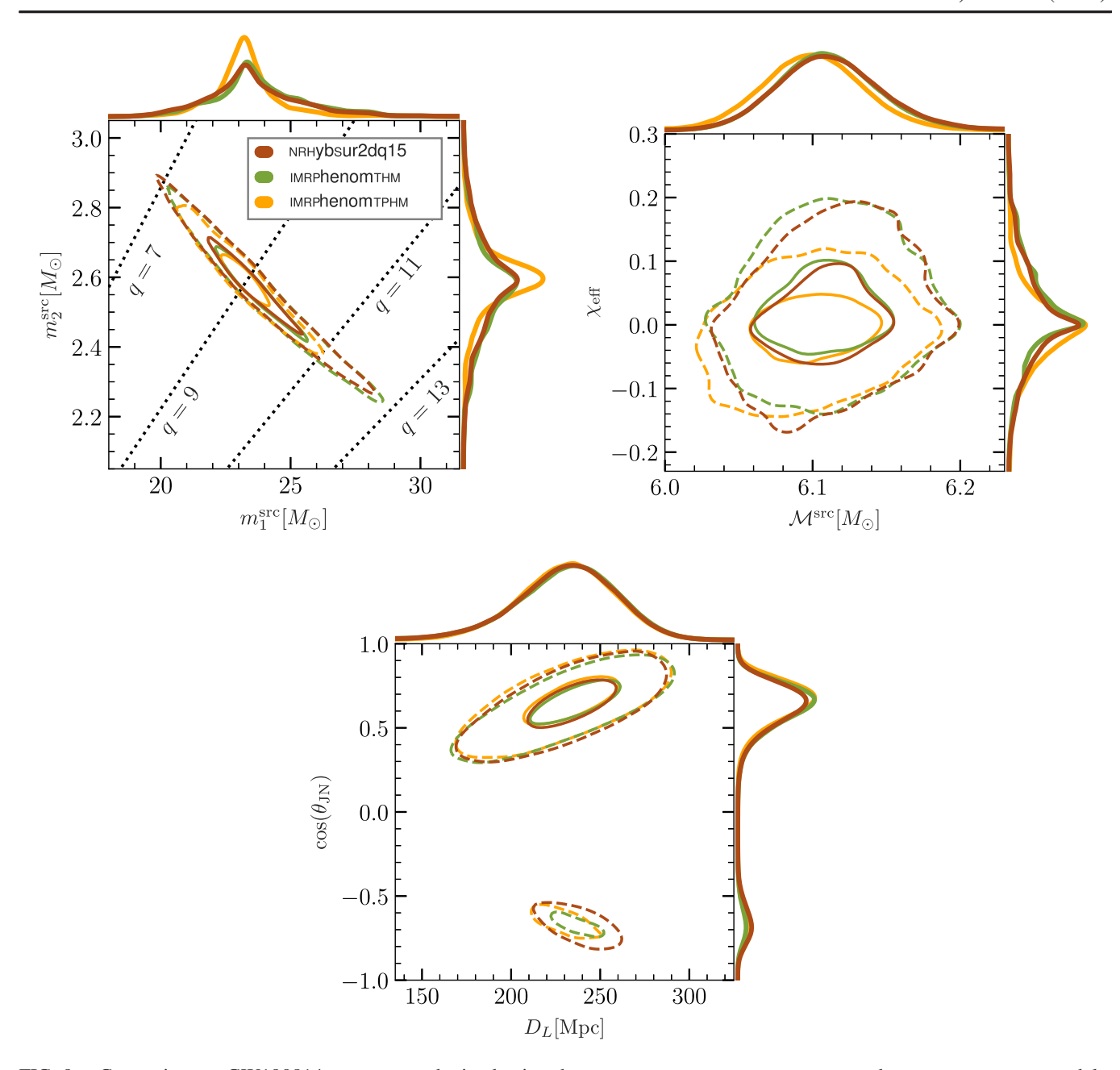


FIG. 9. Constraints on GW190814 parameters obtained using the NRHybsur2dq15, IMRPhenomTHM, and IMRPhenomPv3PHM models. We show posterior distributions for the source-frame component masses $m_1^{\rm src}$ and $m_2^{\rm src}$ (top left), the effective spin $\chi_{\rm eff}$ and the source-frame chirp mass $\mathcal{M}^{\rm src}$ (top right), and the extrinsic parameters $\cos(\theta_{JN})$ and luminosity distance D_L (bottom). The solid (dashed) contours represent the central 50% (90%) credible regions of the joint posteriors. Marginalized 1D posteriors are shown on the plot edges. In the top left panel, we include lines of constant mass ratios (q=7,9,11,13) for comparison. The bimodality in the bottom panel is due to a well-known degeneracy between distance and inclination [97]. IMRPhenomTHM and NRHybsur2dq15 show good agreement, suggesting that IMRPhenomTHM is accurate enough for GW190814-like events at current SNRs. The constraints on the component masses and $\chi_{\rm eff}$ improve for IMRPhenomTPHM compared to the nonprecessing models, suggesting that precession should be included in NRHybSur2dq15.

Source properties can be inferred from GW data following Bayes' theorem (see, e.g., Ref. [88] for a review). We analyze the GW190814 data made public by the LIGO-Virgo-Kagra Collaboration [9,89], using the Parallel Bilby [90] parameter estimation package with the dynesty [91] sampler. Following Ref. [5], we choose a prior that is

uniform in detector frame component masses and isotropic in sky location and binary orientation. For the distance prior, we use the UniformSourceFrame prior [92] assuming a cosmology from [93] as implemented in Astropy [94,95].

When using the nonprecessing models NRHybSur2dq15 and IMRPhenomTHM, we use the AlignedSpin prior [92,96], with

 $-0.5 \le \chi_{1z} \le 0.5$ and $\chi_{2z} = 0$. The AlignedSpin prior follows the generic-spin assumptions of a prior that is uniform in magnitude and isotropic in orientation for each of the two spin vectors, which in the nonprecessing case is projected onto the orbital angular momentum. Even though IMRPhenomTHM allows generic aligned spins on both BHs, we restrict the model to the same spin range as NRHybSur2dq15 for easy comparison. We have, however, verified that using unrestricted aligned spins for IMRPhenomTHM has a negligible impact on GW190814 posteriors; this is expected, as Ref. [9] placed a constraint of $\chi_1 \lesssim 0.07$ at 90% credibility and found that χ_2 cannot be constrained for GW190814. When using the precessing model IMRPhenomTPHM, our prior is uniform in spin magnitudes (with $0 \le \chi_1, \chi_2 \le 1$) and isotropic in spin orientations for both BHs. The reason for considering a precessing model with no spin restrictions is to gauge the impact of neglecting precession in NRHybSur2dq15.

Figure 9 shows posterior distributions for the GW190814 source parameters obtained using NRHybSur2dq15, IMRPhenomTHM, and IMRPhenomTPHM. We show constraints on the source-frame component masses $m_1^{\rm src}$ and $m_2^{\rm src}$, the effective spin $\chi_{\rm eff}$, the source-frame chirp mass $\mathcal{M}^{\rm src} = M^{\rm src} \eta^{3/5}$, the luminosity distance D_L , and cosine of the inclination angle θ_{JN} between the total angular momentum J and the line of sight direction \hat{N} . As NRHybSur2dq15 is significantly more accurate (see Fig. 4), the differences between NRHybSur2dq15 and IMRPhenomTHM can be used to gauge systematic uncertainties in IMRPhenomTHM. In Fig. 9, we find good agreement between NRHybSur2dq15 and IMRPhenomTHM for all parameters shown, which suggests that semianalytical models like IMRPhenomTHM are accurate enough for events like GW190814. However, this may not be the case as detector sensitivity improves and GW190814-like signals are observed at larger SNRs. At larger SNRs, the differences noted in Figs. 4 and 5 can become significant.

Finally, comparing the posteriors for IMRPhenomTHM and IMRPhenomTPHM in Fig. 9, we find that including the effects of precession leads to stronger constraints on the component masses and $\chi_{\rm eff}$, while the chirp mass, distance, and inclination constraints are not significantly affected. This is in agreement with Ref. [9] and implies that precession effects should be included in NRHybSur2dq15. While this can be done by a frame twisting procedure similar to IMRPhenomTPHM, this method does not capture the full effects of precession like the asymmetries between pairs of (ℓ, m) and $(\ell, -m)$ spin-weighted spherical harmonic modes [34,36]. While precessing NR surrogate models [36] capture these effects, they require $\gtrsim 1000$ NR simulations, which are not currently possible at large mass ratios. Therefore, we leave this exploration to future work.

V. CONCLUSION

We present NRHybSur2dq15, a surrogate waveform model targeted at large mass ratio GW events like GW190814. The model is trained on 51 binary BH hybrid waveforms with mass ratios $q \le 15$ and aligned spins $\chi_{1z} \in [-0.5, 0.5]$, $\chi_{2z} = 0$, includes the (2, 2), (2, 1), (3, 3), (4, 4), and (5, 5) spin-weighted spherical harmonic modes, and spans the entire LIGO-Virgo bandwidth (with $f_{low} = 20$ Hz) for total masses $M \gtrsim 9.5~M_{\odot}$. Through a leave-one-out study, we show that NRHybSur2dq15 accurately reproduces the hybrid waveforms, with mismatches below $\sim 2 \times 10^{-3}$ for total masses $10~M_{\odot} \le M \le 300~M_{\odot}$. This is at least an order of magnitude improvement over existing semianalytical models. The model is made publicly available through the easy-to-use PYTHON package GWSurrogate [98].

We reanalyze GW190814 using NRHybSur2dq15 and find results consistent with the discovery paper [9]. This suggests that current semianalytical models are accurate enough for events like GW190814. However, as detector sensitivity improves, we can expect to see similar signals at a higher SNR. We anticipate that accurate models like NRHybSur2dq15 will be necessary for analyzing such signals. With that goal, we identify precession as an important feature to be added to NRHybSur2dq15 in the future.

ACKNOWLEDGMENTS

We thank Hector Estelles and Alessandro Nagar for comments on the manuscript. This work was supported in part by the Sherman Fairchild Foundation and by National Science Foundation (NSF) Grants No. PHY-2011961, No. PHY-2011968, and No. OAC-1931266 at Caltech, and NSF Grants No. PHY-1912081 and No. OAC-1931280 at Cornell. V. V. acknowledges funding from the European Union's Horizon 2020 research and innovation program under the Marie Skłodowska-Curie Grant Agreement No. 896869. V. V. was supported by a Klarman Fellowship at Cornell and also received support from a Marie Curie Fellowship. C.-J. H. acknowledges support of the NSF and the LIGO Laboratory. NR simulations were conducted on the Frontera computing project at the Texas Advanced Computing Center. Additional computations were performed on the Wheeler cluster at Caltech, which is supported by the Sherman Fairchild Foundation and by Caltech, and the High Performance Cluster at Caltech. This material is based upon work supported by NSF's LIGO Laboratory which is a major facility fully funded by the NSF. This research made use of data, software, and/or web tools obtained from the Gravitational Wave Open Science Center [89], a service of the LIGO Laboratory, the LIGO Scientific Collaboration, and the Virgo Collaboration.

- [1] J. Aasi *et al.* (LIGO Scientific Collaboration), Advanced LIGO, Classical Quantum Gravity **32**, 074001 (2015).
- [2] F. Acernese *et al.* (Virgo Collaboration), Advanced Virgo: A second-generation interferometric gravitational wave detector, Classical Quantum Gravity **32**, 024001 (2015).
- [3] B. P. Abbott *et al.* (LIGO Scientific and Virgo Collaborations), GWTC-1: A Gravitational-Wave Transient Catalog of Compact Binary Mergers Observed by LIGO and Virgo during the First and Second Observing Runs, Phys. Rev. X 9, 031040 (2019).
- [4] R. Abbott *et al.* (LIGO Scientific and Virgo Collaborations), GWTC-2.1: Deep extended catalog of compact binary coalescences observed by LIGO and Virgo during the first half of the third observing run, arXiv:2108.01045.
- [5] R. Abbott et al. (LIGO Scientific, Virgo, and KAGRA Collaborations), GWTC-3: Compact binary coalescences observed by LIGO and Virgo during the second part of the third observing run, arXiv:2111.03606.
- [6] B. P. Abbott *et al.* (LIGO Scientific and Virgo Collaborations), Observation of Gravitational Waves from a Binary Black Hole Merger, Phys. Rev. Lett. **116**, 061102 (2016).
- [7] Benjamin P. Abbott *et al.* (LIGO Scientific and Virgo Collaborations), GW170817: Observation of Gravitational Waves from a Binary Neutron Star Inspiral, Phys. Rev. Lett. 119, 161101 (2017).
- [8] R. Abbott et al. (LIGO Scientific, KAGRA, and Virgo Collaborations), Observation of gravitational waves from two neutron star–black hole coalescences, Astrophys. J. Lett. 915, L5 (2021).
- [9] R. Abbott et al. (LIGO Scientific and Virgo Collaborations), GW190814: Gravitational waves from the coalescence of a 23 solar mass black hole with a 2.6 solar mass compact object, Astrophys. J. Lett. 896, L44 (2020).
- [10] Daniel A. Godzieba, David Radice, and Sebastiano Bernuzzi, On the maximum mass of neutron stars and GW190814, Astrophys. J. 908, 122 (2021).
- [11] V. Dexheimer, R. O. Gomes, T. Klähn, S. Han, and M. Salinas, GW190814 as a massive rapidly rotating neutron star with exotic degrees of freedom, Phys. Rev. C 103, 025808 (2021).
- [12] Sebastien Clesse and Juan Garcia-Bellido, GW190425, GW190521 and GW190814: Three candidate mergers of primordial black holes from the QCD epoch, arXiv:2007 .06481.
- [13] Ingo Tews, Peter T. H. Pang, Tim Dietrich, Michael W. Coughlin, Sarah Antier, Mattia Bulla, Jack Heinzel, and Lina Issa, On the nature of GW190814 and its impact on the understanding of supranuclear matter, Astrophys. J. Lett. 908, L1 (2021).
- [14] Antonios Tsokaros, Milton Ruiz, and Stuart L. Shapiro, GW190814: Spin and equation of state of a neutron star companion, Astrophys. J. 905, 48 (2020).
- [15] F. J. Fattoyev, C. J. Horowitz, J. Piekarewicz, and Brendan Reed, GW190814: Impact of a 2.6 solar mass neutron star on the nucleonic equations of state, Phys. Rev. C 102, 065805 (2020).
- [16] Nai-Bo Zhang and Bao-An Li, GW190814's secondary component with mass $2.50-2.67~{\rm M}_{\odot}$ as a superfast pulsar, Astrophys. J. **902**, 38 (2020).

- [17] Hung Tan, Jacquelyn Noronha-Hostler, and Nico Yunes, Neutron Star Equation of State in Light of GW190814, Phys. Rev. Lett. 125, 261104 (2020).
- [18] Antonios Nathanail, Elias R. Most, and Luciano Rezzolla, GW170817 and GW190814: Tension on the maximum mass, Astrophys. J. Lett. 908, L28 (2021).
- [19] Frans Pretorius, Evolution of Binary Black Hole Spacetimes, Phys. Rev. Lett. 95, 121101 (2005).
- [20] Manuela Campanelli, C. O. Lousto, P. Marronetti, and Y. Zlochower, Accurate Evolutions of Orbiting Black-Hole Binaries without Excision, Phys. Rev. Lett. 96, 111101 (2006).
- [21] John G. Baker, Joan Centrella, Dae-II Choi, Michael Koppitz, and James van Meter, Gravitational Wave Extraction from an Inspiraling Configuration of Merging Black Holes, Phys. Rev. Lett. 96, 111102 (2006).
- [22] Michael Boyle *et al.*, The SXS Collaboration catalog of binary black hole simulations, Classical Quantum Gravity **36**, 195006 (2019).
- [23] Serguei Ossokine *et al.*, Multipolar effective-one-body waveforms for precessing binary black holes: Construction and validation, Phys. Rev. D **102**, 044055 (2020).
- [24] Sebastian Khan, Frank Ohme, Katerina Chatziioannou, and Mark Hannam, Including higher order multipoles in gravitational-wave models for precessing binary black holes, Phys. Rev. D **101**, 024056 (2020).
- [25] Andrew Matas *et al.*, Aligned-spin neutron-star–black-hole waveform model based on the effective-one-body approach and numerical-relativity simulations, Phys. Rev. D **102**, 043023 (2020).
- [26] Jonathan E. Thompson, Edward Fauchon-Jones, Sebastian Khan, Elisa Nitoglia, Francesco Pannarale, Tim Dietrich, and Mark Hannam, Modeling the gravitational wave signature of neutron star black hole coalescences, Phys. Rev. D 101, 124059 (2020).
- [27] Roberto Cotesta, Alessandra Buonanno, Alejandro Bohé, Andrea Taracchini, Ian Hinder, and Serguei Ossokine, Enriching the symphony of gravitational waves from binary black holes by tuning higher harmonics, Phys. Rev. D 98, 084028 (2018).
- [28] Héctor Estellés, Marta Colleoni, Cecilio García-Quirós, Sascha Husa, David Keitel, Maite Mateu-Lucena, Maria de Lluc Planas, and Antoni Ramos-Buades, New twists in compact binary waveform modeling: A fast time domain model for precession, Phys. Rev. D 105, 084040 (2022).
- [29] Héctor Estellés, Sascha Husa, Marta Colleoni, David Keitel, Maite Mateu-Lucena, Cecilio García-Quirós, Antoni Ramos-Buades, and Angela Borchers, Time domain phenomenological model of gravitational wave subdominant harmonics for quasicircular nonprecessing binary black hole coalescences, Phys. Rev. D 105, 084039 (2022).
- [30] Geraint Pratten et al., Computationally efficient models for the dominant and subdominant harmonic modes of precessing binary black holes, Phys. Rev. D 103, 104056 (2021).
- [31] Cecilio García-Quirós, Marta Colleoni, Sascha Husa, Héctor Estellés, Geraint Pratten, Antoni Ramos-Buades, Maite Mateu-Lucena, and Rafel Jaume, Multimode frequency-domain model for the gravitational wave signal from nonprecessing black-hole binaries, Phys. Rev. D 102, 064002 (2020).

- [32] Sarp Akcay, Rossella Gamba, and Sebastiano Bernuzzi, Hybrid post-Newtonian effective-one-body scheme for spin-precessing compact-binary waveforms up to merger, Phys. Rev. D 103, 024014 (2021).
- [33] Alessandro Nagar, Gunnar Riemenschneider, Geraint Pratten, Piero Rettegno, and Francesco Messina, Multipolar effective one body waveform model for spin-aligned black hole binaries, Phys. Rev. D 102, 024077 (2020).
- [34] Vijay Varma, Maximiliano Isi, Sylvia Biscoveanu, Will M. Farr, and Salvatore Vitale, Measuring binary black hole orbital-plane spin orientations, Phys. Rev. D 105, 024045 (2022).
- [35] Vijay Varma, Scott E. Field, Mark A. Scheel, Jonathan Blackman, Lawrence E. Kidder, and Harald P. Pfeiffer, Surrogate model of hybridized numerical relativity binary black hole waveforms, Phys. Rev. D 99, 064045 (2019).
- [36] Vijay Varma, Scott E. Field, Mark A. Scheel, Jonathan Blackman, Davide Gerosa, Leo C. Stein, Lawrence E. Kidder, and Harald P. Pfeiffer, Surrogate models for precessing binary black hole simulations with unequal masses, Phys. Rev. Research 1, 033015 (2019).
- [37] S. E. Field, C. R. Galley, J. S. Hesthaven, J. Kaye, and M. Tiglio, Fast Prediction and Evaluation of Gravitational Waveforms Using Surrogate Models, Phys. Rev. X 4, 031006 (2014).
- [38] Jonathan Blackman, Scott E. Field, Mark A. Scheel, Chad R. Galley, Christian D. Ott, Michael Boyle, Lawrence E. Kidder, Harald P. Pfeiffer, and Béla Szilágyi, Numerical relativity waveform surrogate model for generically precessing binary black hole mergers, Phys. Rev. D 96, 024058 (2017).
- [39] Carlos O. Lousto and James Healy, Exploring the Small Mass Ratio Binary Black Hole Merger via Zeno's Dichotomy Approach, Phys. Rev. Lett. 125, 191102 (2020).
- [40] R. Abbott et al. (LIGO Scientific, Virgo, and KAGRA Collaborations), The population of merging compact binaries inferred using gravitational waves through GWTC-3, arXiv:2111.03634.
- [41] Vijay Varma and Parameswaran Ajith, Effects of nonquadrupole modes in the detection and parameter estimation of black hole binaries with nonprecessing spins, Phys. Rev. D 96, 124024 (2017).
- [42] Vijay Varma, Parameswaran Ajith, Sascha Husa, Juan Calderon Bustillo, Mark Hannam, and Michael Pürrer, Gravitational-wave observations of binary black holes: Effect of nonquadrupole modes, Phys. Rev. D 90, 124004 (2014).
- [43] Collin Capano, Yi Pan, and Alessandra Buonanno, Impact of higher harmonics in searching for gravitational waves from nonspinning binary black holes, Phys. Rev. D 89, 102003 (2014).
- [44] Feroz H. Shaik, Jacob Lange, Scott E. Field, Richard O'Shaughnessy, Vijay Varma, Lawrence E. Kidder, Harald P. Pfeiffer, and Daniel Wysocki, Impact of subdominant modes on the interpretation of gravitational-wave signals from heavy binary black hole systems, Phys. Rev. D 101, 124054 (2020).
- [45] Tousif Islam, Scott E. Field, Carl-Johan Haster, and Rory Smith, High precision source characterization of intermediate mass-ratio black hole coalescences with gravitational

- waves: The importance of higher order multipoles, Phys. Rev. D **104**, 084068 (2021).
- [46] The Spectral Einstein Code, http://www.black-holes.org/ SpEC.html.
- [47] Simulating Extreme Spacetimes, http://www.black-holes.org/.
- [48] Theocharis A. Apostolatos, Curt Cutler, Gerald J. Sussman, and Kip S. Thorne, Spin-induced orbital precession and its modulation of the gravitational waveforms from merging binaries, Phys. Rev. D **49**, 6274 (1994).
- [49] P. Schmidt, F. Ohme, and M. Hannam, Towards models of gravitational waveforms from generic binaries II: Modelling precession effects with a single effective precession parameter, Phys. Rev. D 91, 024043 (2015).
- [50] Jonathan Blackman, Scott E. Field, Mark A. Scheel, Chad R. Galley, Daniel A. Hemberger, Patricia Schmidt, and Rory Smith, A surrogate model of gravitational waveforms from numerical relativity simulations of precessing binary black hole mergers, Phys. Rev. D 95, 104023 (2017).
- [51] Eanna E. Flanagan and Tanja Hinderer, Constraining neutron star tidal Love numbers with gravitational wave detectors, Phys. Rev. D 77, 021502 (2008).
- [52] Francois Foucart, Luisa Buchman, Matthew D. Duez, Michael Grudich, Lawrence E. Kidder, Ilana MacDonald, Abdul Mroue, Harald P. Pfeiffer, Mark A. Scheel, and Bela Szilagyi, First direct comparison of nondisrupting neutron star-black hole and binary black hole merger simulations, Phys. Rev. D 88, 064017 (2013).
- [53] Michael Boyle, GWFrames, https://github.com/moble/ GWFrames.
- [54] Michael Boyle, Duncan A. Brown, Lawrence E. Kidder, Abdul H. Mroue, Harald P. Pfeiffer, Mark A. Scheel, Gregory B. Cook, and Saul A. Teukolsky, High-accuracy comparison of numerical relativity simulations with post-Newtonian expansions, Phys. Rev. D 76, 124038 (2007).
- [55] Luc Blanchet, Thibault Damour, Gilles Esposito-Farese, and Bala R. Iyer, Gravitational Radiation from Inspiralling Compact Binaries Completed at the Third Post-Newtonian Order, Phys. Rev. Lett. **93**, 091101 (2004).
- [56] Piotr Jaranowski and Gerhard Schäfer, Dimensional regularization of local singularities in the 4th post-Newtonian two-point-mass Hamiltonian, Phys. Rev. D 87, 081503 (2013).
- [57] Donato Bini and Thibault Damour, Analytical determination of the two-body gravitational interaction potential at the fourth post-Newtonian approximation, Phys. Rev. D 87, 121501 (2013).
- [58] Donato Bini and Thibault Damour, High-order post-Newtonian contributions to the two-body gravitational interaction potential from analytical gravitational selfforce calculations, Phys. Rev. D **89**, 064063 (2014).
- [59] Lawrence E. Kidder, Coalescing binary systems of compact objects to post-Newtonian 5/2 order. V. Spin effects, Phys. Rev. D 52, 821 (1995).
- [60] Clifford M. Will and Alan G. Wiseman, Gravitational radiation from compact binary systems: Gravitational wave forms and energy loss to second post-Newtonian order, Phys. Rev. D 54, 4813 (1996).
- [61] Alejandro Bohe, Sylvain Marsat, Guillaume Faye, and Luc Blanchet, Next-to-next-to-leading order spin-orbit effects in

- the near-zone metric and precession equations of compact binaries, Classical Quantum Gravity **30**, 075017 (2013).
- [62] Luc Blanchet, Guillaume Faye, Bala R. Iyer, and Siddhartha Sinha, The third post-Newtonian gravitational wave polarisations and associated spherical harmonic modes for inspiralling compact binaries in quasi-circular orbits, Classical Quantum Gravity 25, 165003 (2008); 29, 239501(E) (2012).
- [63] Guillaume Faye, Sylvain Marsat, Luc Blanchet, and Bala R. Iyer, The third and a half post-Newtonian gravitational wave quadrupole mode for quasi-circular inspiralling compact binaries, Classical Quantum Gravity 29, 175004 (2012).
- [64] Guillaume Faye, Luc Blanchet, and Bala R. Iyer, Non-linear multipole interactions and gravitational-wave octupole modes for inspiralling compact binaries to third-and-a-half post-Newtonian order, Classical Quantum Gravity 32, 045016 (2015).
- [65] SXS Collaboration, The SXS Collaboration Catalog of gravitational waveforms, http://www.black-holes.org/ waveforms.
- [66] James W. York, Jr., Conformal "Thin Sandwich" Data for the Initial-Value Problem, Phys. Rev. Lett. 82, 1350 (1999).
- [67] Harald P. Pfeiffer and James W. York, Jr., Extrinsic curvature and the Einstein constraints, Phys. Rev. D 67, 044022 (2003).
- [68] Vijay Varma, Mark A. Scheel, and Harald P. Pfeiffer, Comparison of binary black hole initial data sets, Phys. Rev. D 98, 104011 (2018).
- [69] Lee Lindblom, Mark A. Scheel, Lawrence E. Kidder, Robert Owen, and Oliver Rinne, A new generalized harmonic evolution system, Classical Quantum Gravity 23, S447 (2006).
- [70] Oliver Rinne, Luisa T. Buchman, Mark A. Scheel, and Harald P. Pfeiffer, Implementation of higher-order absorbing boundary conditions for the Einstein equations, Classical Quantum Gravity **26**, 075009 (2009).
- [71] Alessandra Buonanno, Lawrence E. Kidder, Abdul H. Mroue, Harald P. Pfeiffer, and Andrea Taracchini, Reducing orbital eccentricity of precessing black-hole binaries, Phys. Rev. D 83, 104034 (2011).
- [72] Michael Boyle and Abdul H. Mroue, Extrapolating gravitational-wave data from numerical simulations, Phys. Rev. D 80, 124045 (2009).
- [73] Charles J. Woodford, Michael Boyle, and Harald P. Pfeiffer, Compact binary waveform center-of-mass corrections, Phys. Rev. D 100, 124010 (2019).
- [74] Alejandro Bohé et al., Improved effective-one-body model of spinning, nonprecessing binary black holes for the era of gravitational-wave astrophysics with advanced detectors, Phys. Rev. D 95, 044028 (2017).
- [75] Thibault Damour, Bala R. Iyer, and B. S. Sathyaprakash, A comparison of search templates for gravitational waves from binary inspiral, Phys. Rev. D 63, 044023 (2001); 72, 029902 (E) (2005).
- [76] Alessandra Buonanno, Bala Iyer, Evan Ochsner, Yi Pan, and B. S. Sathyaprakash, Comparison of post-Newtonian templates for compact binary inspiral signals in gravitationalwave detectors, Phys. Rev. D 80, 084043 (2009).

- [77] Vijay Varma, Ryuichi Fujita, Ashok Choudhary, and Bala R. Iyer, Comparison of post-Newtonian templates for extreme mass ratio inspirals, Phys. Rev. D 88, 024038 (2013).
- [78] Scott E. Field, Chad R. Galley, Frank Herrmann, Jan S. Hesthaven, Evan Ochsner, and Manuel Tiglio, Reduced Basis Catalogs for Gravitational Wave Templates, Phys. Rev. Lett. 106, 221102 (2011).
- [79] Maxime Barrault, Yvon Maday, Ngoc Cuong Nguyen, and Anthony T. Patera, An "empirical interpolation" method: Application to efficient reduced-basis discretization of partial differential equations, C. R. Math. 339, 667 (2004).
- [80] Y. Maday, N. C. Nguyen, A. T. Patera, and S. H. Pau, A general multipurpose interpolation procedure: The magic points, Commun. Pure Appl. Anal. **8**, 383 (2009).
- [81] Jan S. Hesthaven, Benjamin Stamm, and Shun Zhang, Efficient greedy algorithms for high-dimensional parameter spaces with applications to empirical interpolation and reduced basis methods, ESAIM: M2AN 48, 259 (2014).
- [82] Vijay Varma, Davide Gerosa, Leo C. Stein, François Hébert, and Hao Zhang, High-Accuracy Mass, Spin, and Recoil Predictions of Generic Black-Hole Merger Remnants, Phys. Rev. Lett. 122, 011101 (2019).
- [83] Afura Taylor and Vijay Varma, Gravitational wave peak luminosity model for precessing binary black holes, Phys. Rev. D 102, 104047 (2020).
- [84] P. Ajith, Addressing the spin question in gravitational-wave searches: Waveform templates for inspiralling compact binaries with nonprecessing spins, Phys. Rev. D 84, 084037 (2011).
- [85] Nur E. M. Rifat, Scott E. Field, Gaurav Khanna, and Vijay Varma, Surrogate model for gravitational wave signals from comparable and large-mass-ratio black hole binaries, Phys. Rev. D **101**, 081502 (2020).
- [86] Alessandro Nagar, James Healy, Carlos O. Lousto, Sebastiano Bernuzzi, and Angelica Albertini, Numericalrelativity validation of effective-one-body waveforms in the intermediate-mass-ratio regime, Phys. Rev. D 105, 124061 (2022).
- [87] LIGO Scientific Collaboration, Updated Advanced LIGO sensitivity design curve, Technical Report, 2018, https://dcc.ligo.org/LIGO-T1800044/public.
- [88] Eric Thrane and Colm Talbot, An introduction to Bayesian inference in gravitational-wave astronomy: Parameter estimation, model selection, and hierarchical models, Publ. Astron. Soc. Aust. **36**, e010 (2019).
- [89] LIGO Scientific and Virgo Collaborations, Gravitational Wave Open Science Center, https://www.gw-openscience.org.
- [90] Rory J. E. Smith, Gregory Ashton, Avi Vajpeyi, and Colm Talbot, Massively parallel Bayesian inference for transient gravitational-wave astronomy, Mon. Not. R. Astron. Soc. 498, 4492 (2020).
- [91] Joshua S. Speagle, DYNESTY: A dynamic nested sampling package for estimating Bayesian posteriors and evidences, Mon. Not. R. Astron. Soc. **493**, 3132 (2020).
- [92] I. M. Romero-Shaw *et al.*, Bayesian inference for compact binary coalescences with bilby: Validation and application to the first LIGO–Virgo gravitational-wave transient catalogue, Mon. Not. R. Astron. Soc. **499**, 3295 (2020).

- [93] P. A. R. Ade *et al.* (Planck Collaboration), Planck 2015 results. XIII. Cosmological parameters, Astron. Astrophys. 594, A13 (2016).
- [94] Thomas P. Robitaille *et al.* (Astropy Collaboration), Astropy: A community python package for astronomy, Astron. Astrophys. **558**, A33 (2013).
- [95] A. M. Price-Whelan *et al.* (Astropy Collaboration), The Astropy project: Building an open-science project and status of the v2.0 core package, Astron. J. **156**, 123 (2018).
- [96] T. Callister, A thesaurus for common priors in gravitationalwave astronomy, arXiv:2104.09508.
- [97] Curt Cutler and Eanna E. Flanagan, Gravitational waves from merging compact binaries: How accurately can one extract the binary's parameters from the inspiral wave form?, Phys. Rev. D **49**, 2658 (1994).
- [98] Jonathan Blackman, Scott Field, Chad Galley, and Vijay Varma, GWSurrogate, https://pypi.python.org/pypi/gwsurrogate/.